Design, fabrication and testing of a serial kinematic MEMS *XY* stage for multifinger manipulation

Yong-Sik Kim[1,2,4]**, Jae-Myung Yoo**[1]**, Seung Ho Yang**[1]**,**
Young-Man Choi[1,3]**, Nicholas G Dagalakis**[1] **and Satyandra K Gupta**[2]

[1] Intelligent System Division, Engineering Laboratory, National Institute of Standards and Technology,
100 Bureau Dr. Gaithersburg, MD, 20899, USA
[2] Department of Mechanical Engineering and Institute for Systems Research, University of Maryland,
College Park, Maryland, 20742, USA
[3] Korea Institute for Machinery and Materials, 156 Gajeongbuk-Ro, Yuseong-Gu, Daejeon, Korea

E-mail: mk37do@gmail.com

Abstract

In micro-electro-mechanical systems (MEMS) it is difficult to obtain a large range of motion with a small coupled error. This limitation was overcome by designing and fabricating a nested structure as a serial kinematic mechanism (SKM). In this paper, a MEMS-based *XY* stage is reported for multifinger manipulation application. The SKM MEMS *XY* stage is implemented by embedding a single degree-of-freedom (DOF) stage into another single DOF stage. The proposed MEMS *XY* stage is fabricated by deep reactive ion etching (DRIE) from both sides of a silicon-on-insulator (SOI) wafer. This SKM MEMS stage has the capability to generate more than 50 μm displacements along each *X*- and *Y*-axes. This nested structure also suppressed the coupled motion error to 0.6% of the original actuation displacement. For the demonstration on the micro-particle manipulation, a 15 μm sized polypropylene particle is manipulated and rotated by operating two individual fingers attached to proposed MEMS stages.

(Some figures may appear in colour only in the online journal)

1. Introduction

A precision-positioning stage is used to move an end-effector in its work space to a desired position precisely within allowable degrees-of-freedom (DOF). The end-effector is a device such as a probe tip, a gripper, or a test bed, connected to the positioning stage to interact with external environments. The stage can be evaluated by basic features such as range of motion, coupled motion error and resolution. Various stage designs have been investigated to achieve a large range of motion with acceptable coupled motion error based on a reasonable stage size [1]. Micro-electro-mechanical system (MEMS) approaches have the great advantage of having a small footprint, which then increases the integration capability to external

applications [2]. Hence, MEMS-positioning stages have been widely used in many applications such as optical systems [3, 4], atomic force microscopes (AFMs) [5] and nano-manufacturing assembly [6, 7].

An important design goal for a MEMS XY stage is to maximize the range of motion for one DOF without causing intended motion in the other DOF (called coupled motion error). Various approaches have been tried to improve in-plane 2 DOF in the stage design using existing MEMS fabrication techniques. One of the approaches is aligning two actuators along *X*- and *Y*-axes and then connecting them to the end-effector directly as parallel kinematic mechanisms (PKMs) [8]. But this results in a reduction in the range of motion to 17 μm × 11 μm, and an increase in the coupled error between the actuators. To overcome the coupled motion error, an accurate mathematical kinematic model or additional kinematic features are necessary. This leads to

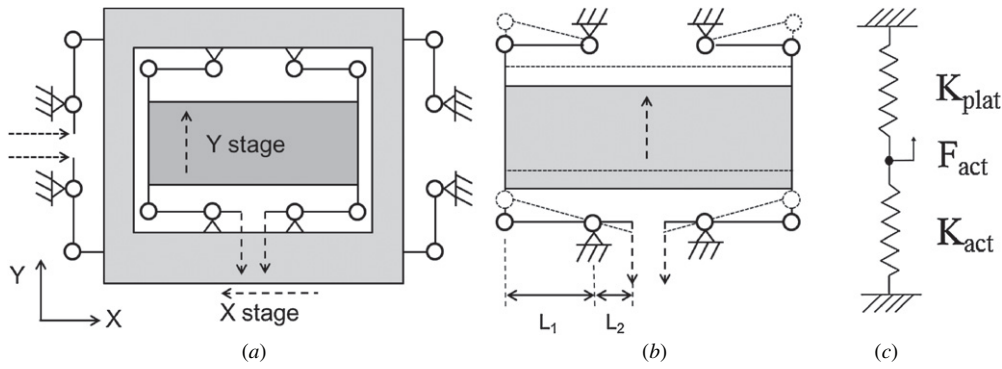[4] Author to whom any correspondence should be addressed.

Figure 1. (*a*) Schematic diagram of the *XY* stage; (*b*) schematic figure of the chosen single DOF stage; (*c*) free-body diagram of the single DOF stage in (*b*).

nonlinear kinematics models, which are difficult to analyze. One commonly used as a compensating structure in PKM is parallel four-bar chains, which reduce the unwanted motion such as rotations at the end-effector [9, 10]. However, this type of additional feature causes an increase in stiffness resulting in a shorter range of motion. In addition, the systems adopting PKM with four-bar chains still suffer from coupled motion error. This coupled motion error is overcome by using features such as leaf springs [10]. But the use of leaf springs leads to reduction in the range of motion.

A serial kinematic mechanism (SKM) is an alternative approach [11], wherein each link is connected to only two neighboring links like welding robot arms. The displacement of the end-effector can be expressed by accumulation of each moving component. Since there are no mechanical structures coupled between specified DOFs, each actuator in a SKM is expected to generate its original range of motion with acceptable coupled motion error. Compared with PKMs, SKMs have (a) easy-to-solve forward kinematics, (b) high dexterity and (c) no reduction in the range of motion when multiple actuators are combined [1]. However, the implementation of SKMs in MEMS is a challenge, because the stacking up of single DOF stages requires structures in height, which is difficult to implement with a planar design approach. Moreover, electrical access to each moving component without disturbing others should be taken into consideration.

Other important features in MEMS stages are flexure hinges and actuators. Flexure hinges have been used in various MEMS applications [1, 7, 10, 11] due to the fact that they are free of backlash and are of monolithic design. Electrostatic [9, 10], electromagnetic [12] and electrothermal actuators [13] have been widely used for positioning the end-effector. Among them, electrothermal actuators can generate a relatively stronger force compared to other types of actuators. A high-force magnitude is crucial in pushing or pulling external mechanical loads.

This study focuses on the design, fabrication and test of a MEMS *XY* stage based on a SKM. The SKM is realized with a nested structure by embedding a single DOF stage into the other. With this approach, two DOF in-plane motions of the end effector can be generated. In this study, a single DOF stage design was modified for long-range motion in excess of 50 μm.

2. Design of the *XY* stage

The proposed MEMS *XY* stage is composed of two single DOF stages. In the *XY* stage, one single DOF stage is aligned to the *X*-axis (called an *X* stage) and the other is aligned along the *Y*-axis (called a *Y* stage) as shown in figure 1(*a*), where the arrows indicate the direction of the actuator motion. The *X* stage corresponds to the *X*-axis motion of the end-effector and the *Y* stage to the *Y*-axis motion. The *Y* stage is fully embedded into the *X* stage as a SKM. This nested structure is able to combine two individual stages into one device for two DOF motions and isolate one actuation motion from the other for reducing coupled motion error. The end-effector will be a platform of the *Y* stage in this case and is linked to a fixed ground through the neighboring *Y* stage and the *X* stage in a sequence. The chosen single DOF stage is made up of an actuator, a platform and links as shown in figure 1(*b*) [13]. The white circles in figures 1(*a*) and (*b*) represent flexure hinges which are used as joints and solid lines stand for links connecting the actuator to the platform. The electrothermal actuator is connected to two levers for the amplification of the displacement, which is adjustable by selecting L_1 and L_2.

The single DOF stage (figure 1(*b*)) is represented by the free-body diagram (figure 1(*c*)), where K_{act} and K_{plat} stand for the stiffness of the actuator and the platform, respectively. F_{act} is the force generated by the actuator. Based on this diagram, the expected displacement of the platform can be expressed as

$$U_{plat} = \left(\frac{L_1}{L_2}\right) U_{act} = \left(\frac{L_1}{L_2}\right) \frac{F_{act}}{K_{act} + K_{plat}} \qquad (1)$$

where U_{act} and U_{plat} stand for the displacement of the actuator and the platform, respectively. Each term in equation (1) is analyzed in following sections.

2.1. The MEMS design of the SKM

The implementation of the *XY* stage requires several additional features in order to combine two individual stages into one system without significant coupled motion error. First, the two single DOF stages should be electrically isolated. Otherwise, the electric leaking may exacerbate the coupled motion error. Second, the *Y* stage needs an appropriate electrical connection from outside. Without appropriate electrical connection,
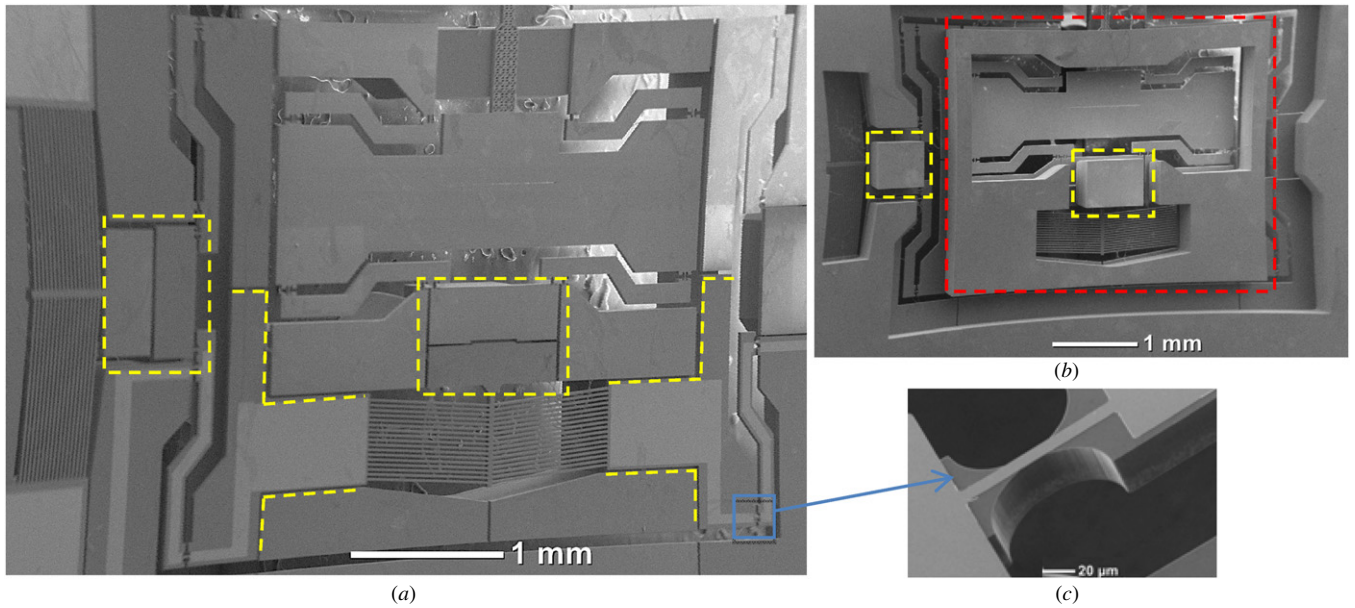
Figure 2. Scanning electron micrographs of the SKM *XY* stage: (*a*) a full view of the fabricated *XY* stage; (*b*) a backside frame to hold the *Y* stage and two connecting blocks for electric isolation; (*c*) an electric path over the flexure hinge.

general wire bonding can damage the *Y* stage or interfere with the stage motion. Third, both ends of electrothermal actuator in the *Y* stage should keep a constant distance from each other during the operation. If not, some of the actuator force is consumed to move those ends, not for the end-effector.

In order to implement the features described above, a dual layer structure was adopted, which was implemented by utilizing both sides of silicon-on-insulator (SOI) wafers. The SOI wafers consist of three layers: a top silicon layer (called device layer), a substrate silicon layer (called handle layer) and a buried oxide layer between them. With SOI wafers, the separated structures in the device layer can hold their positions by connecting them through the device layer. Due to the buried oxide layer between them, the gaps operate as electrical and thermal insulation. This additional feature also works as anchors to hold both ends of the actuator in position. Based on this dual-layer approach, the proposed *XY* stage is fabricated and is shown in figure 2(*a*). The electrical isolation is shown in yellow boxes in figure 2(*a*), where physical gaps are supported by blocks in yellow boxes in figure 2(*b*). The electric path is also isolated from the other actuator by physical gaps which are shown in yellow dotted lines in figure 2(*a*). These gaps are also held by the backside frame shown in the red box in figure 2(*b*). This backside frame also works as the anchor to hold both ends of the actuator in the *Y* stage.

For the electrical connection to the *Y* stage, thin metal layers were deposited from the outside metal pad through the levers and flexures. A detailed view of the electrical connection over the flexure hinge is shown in figure 2(*c*). With this seamless connection, the *Y* stage can be electrically connected to the metal pad which is on firm ground and is available for wire bonding.

2.2. The mathematical analysis for the chosen single DOF stage

A previously reported single DOF stage has a maximum displacement of 12 μm and a resolution of 12 nm [13], which is not enough for manipulation of micro particles. For a longer range of motion, the design of the single DOF stage needs to be modified. One of the advantages of an SKM is that all components, except interfaces to adjacent components, can be modified without redesigning the whole SKM. As the coupled motion error can be decreased by adapting an SKM as described in the previous section, a longer range of motion can be achieved by modifying the single DOF stage separately. Analytic relationships were developed in this section and design parameters were modified.

2.2.1. The electrothermal actuator.
Figure 3(*a*) shows the schematic diagram of the electrothermal actuator. This actuator is known as a bent-beam electrothermal actuator. Thermally expanded beams in the actuator generate one-directional force, F_{act}, due to the bent angle.

The design parameters in the actuator are beam length (L), beam width (W), angle (θ), number of beams (n), and beam thickness (T) and are shown in figures 3(*a*) and (*b*). Some of them have design constrains: (*a*) beam thickness (T) is predefined by the wafer thickness. (*b*) Beam length (L) is limited by link length (L_1) (figure 1(*b*)). A longer L leads to a longer range of motion. But if L is longer than L_1, then the actuator will have to be bigger than the platform resulting in excess area around the platform. Therefore, L is set to be equal to L_1. (*c*) The number of beams (n) is associated with the stiffness of the actuator and lever ratio, explained in section 2.2.3. (*d*) The beam width (W) should be smaller than T to avoid any out-of-plane bending or buckling prior to in-plane motion. (*e*) All parameters should be greater than 10% of T due to the 1:10 high-aspect ratio from the Bosch deep reactive
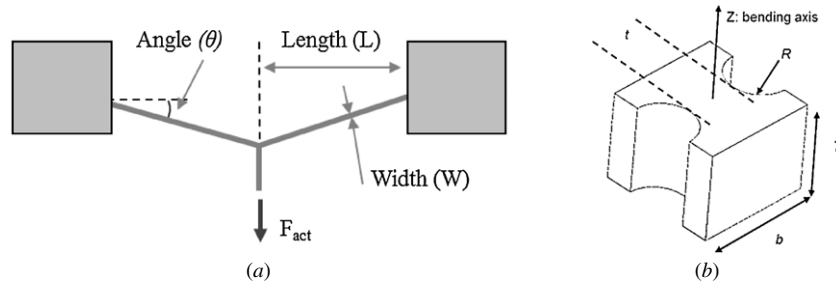
Figure 3. (*a*) Schematic diagram of the electrothermal actuator; (*b*) a schematic of flexure hinge (*t*: flexure neck width, *R*: radius of curvature, *b*: flexure width).

ion etching (DRIE) process [17]. With the above-mentioned parameters, the following analytic relationships were derived.

The stiffness of the electrothermal actuator (K_{act}) in equation (1) can be expressed [18] as

$$K_{act} = 2n\left(\sin^2\theta + \cos^2\theta\frac{12I}{AL^2}\right)\frac{EWT}{L} \qquad (2)$$

where E is the Young's modulus of silicon, and I is the area moment of inertia. The force generated by the actuator is calculated from beam theory as

$$F_{act} = 2\alpha n\Delta T_{ave}EWT\sin\theta \qquad (3)$$

where α is the coefficient of thermal expansion of silicon and ΔT_{ave} is the average temperature rise of the actuator.

2.2.2. The flexure hinge design. The actuator is connected to the platform via flexure hinges as shown in figure 1(*b*). The flexure hinges are compliant mechanisms transmitting rotational motion via their elastic deformation. The stiffness of the platform, K_{plat}, can be expressed by the combination of the compliance of the flexure hinges and the lever ratio as

$$K_{plat} = \frac{m}{L_1^2 C_z} \qquad (4)$$

where m is a number of flexure hinges, L_1 is the link lengths shown in figure 1(*b*), and C_z is its angular compliance about the Z-axis of the flexure hinge [14]. A narrower flexure neck width (t) leads to higher C_z and can produce a longer displacement, but this makes the flexure hinges weak during fabrication. On considering the fabrication yields and stiffness of the flexure hinges, 7 μm was selected as the optimum flexure neck width (t). The flexure hinge thickness (T) was set to be 30 μm, which is the SOI wafer thickness used in fabrication. The radius of curvature (R) was set to be 40 μm and the flexure width (b) was obtained from the relationship $b = 2R + t$. Using equation (4) the rotational stiffness of the selected flexure hinge design and the linear stiffness of the platform, K_{plat}, were found to be 7.52 Nm μrad^{-1} and 46.28 N m^{-1}, respectively.

2.2.3. The lever ratio and the number of beams. The schematic diagram of the lever, the actuator and the platform is shown in figure 4(*a*).

The force balance from the lever mechanism gives

$$\left(\frac{L_1}{L_2}\right)^2 K_{plat}U_{act} = nF_{act} - K_{act}U_{act} \qquad (5)$$

Table 1. The dimensional range of the design parameters.

Symbol	Design parameter	Values
W	Actuator beam width	22.3 μm
θ	Actuator beam angle	0.068 rad
L	Actuator beam length	1000 μm
T	Actuator beam thickness	30 μm
n	Number of beams in actuator	15
L_1	Link length	1000 μm
L_2	Short link length	100 μm
m	Links connected to the platform	8
t	Flexure hinge neck width	7 μm
b	Flexure hinge width	87 μm
R	Flexure hinge radius of curvature	40 μm
ΔT_{ave}	Actuator average temperature	<550 °C
ΔT_{max}	Actuator maximum temperature	<550 °C
U_{plat}	Platform displacement	>50 μm
K_{act}	Actuator stiffness with a single beam	889.16 N m^{-1}
K_{plat}	Platform stiffness without the levers	46.28 N m^{-1}
$F_{act,max}$	Maximum generated force by the actuator with 15 beams	125.3 mN

where L_1/L_2 is the lever ratio, U_{act} is the input displacement from the actuator, F_{act} is a force generated from a single beam in the actuator. Equation (5) can be rearranged for the actuator displacement as

$$U_{act} = \frac{nF_{act}}{\left(\frac{L_1}{L_2}\right)^2 K_{plat} + K_{act}}. \qquad (6)$$

U_{plat} can be expressed by U_{act} and the lever ratio as

$$U_{plat} = \left(\frac{L_1}{L_2}\right)U_{act} = \left(\frac{L_1}{L_2}\right)\frac{nF_{act}}{\left(\frac{L_1}{L_2}\right)^2 K_{plat} + K_{act}}. \qquad (7)$$

Figure 4(*b*) is plotted based on equation (7) to obtain the relationship between different 'n' and lever ratio (L_1/L_2), where K_{act} is obtained from equation (2) with maximum allowable temperature, F_{act} from equation (3) and K_{plat} from equation (4) with the values listed in table 1. This diagram shows that the increase in the number of beams results in an increase in the range of motion. Further, a different number
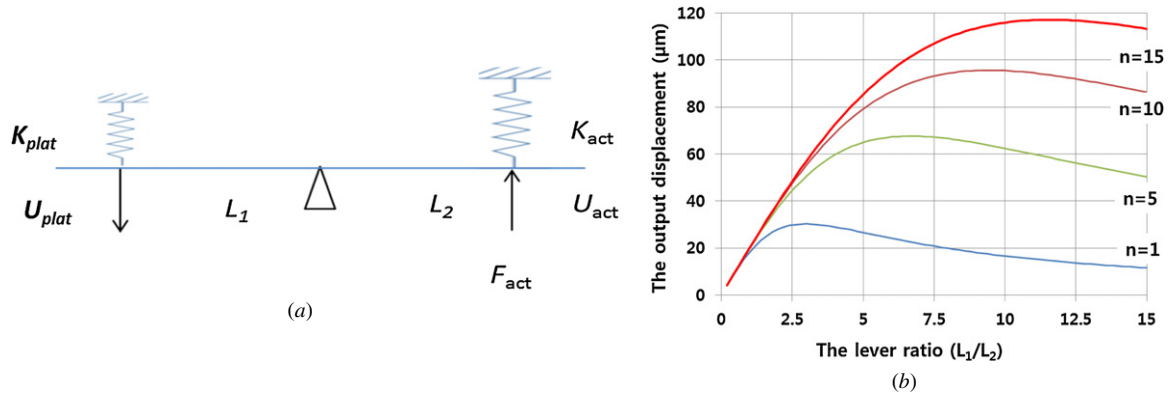
Figure 4. The lever mechanism: (*a*) schematic diagram; (*b*) maximum elastic displacement via lever ratio.

of beams has its own optimum lever ratio which shows the maximum output displacement. With limited space in the *Y* stage, it is difficult to increase the number of beams to more than 15 and higher than 1:10 lever ratio. Thus 15 beams and 1:10 lever ratio were selected in the stage design and, as a result, a displacement of 115 μm is possible at the platform based on equation (7). But this is limited by other design constraints such as thermal and structural issues.

2.2.4. Design constraints: thermal melting and buckling. When the maximum temperature of the electrothermal actuator is below 550 °C, the actuator could be very stable and the predicted output displacement matches well with the experimental data [19]. Therefore, it is necessary to operate the actuators under 550 °C. The temperature distribution along the beam can be expressed [20] as

$$k\frac{d^2T}{dx^2} + \left(\frac{V}{\rho L}\right)^2 \rho = 0 \text{ for } -L \leqslant x \leqslant L. \quad (8)$$

The solution for equation (8) can be expressed as

$$\Delta T(x) = \frac{V^2}{2k\rho L^2}(L^2 - x^2) \text{ for } -L \leqslant x \leqslant L \quad (9)$$

where *V* is an applied voltage, *k* is the thermal conductivity and ρ is the resistivity of silicon. The resistivity (ρ) varies with the applied voltage since the temperature of the electrothermal actuator increases with the applied voltage. The measured resistivity as a function of the applied voltage was: $\rho = -5 \times 10^{-5}(\Omega \text{ m V}^{-1})V + 0.0004 \text{ (}\Omega \text{ m)}$, where *V* is the applied voltage. The range of the temperature was 20–550 °C and the average value of the measured resistivity was 0.000 275 Ω m. The maximum temperature change, $\Delta T_{\max}$, and the average temperature change, ΔT_{ave}, of the electrothermal actuator are derived from equation (9) and expressed as

$$\Delta T_{\text{ave}} = \int_{-L}^{L} \frac{\Delta T(x)}{2L} dx = \frac{V^2}{3k\rho} \quad (10)$$

$$\Delta T_{\max} = \frac{V^2}{2k\rho} = \frac{3}{2}\Delta T_{\text{ave}} < 530 \text{ °C}. \quad (11)$$

The maximum allowable temperature change $\Delta T_{\max}$ from a room temperature 20 °C in equation (11) should not exceed 530 °C to prevent any thermal issues. From equation (11) and

corresponding resistivity, it was found that the applied voltage, *V*, should be less than 5.38 V.

The buckling of the actuator beam is also important and considered thoroughly. When the buckling occurs, the force generated by the actuator is consumed as a form of deformation of the actuator beams. The boundary condition of the bent-beam type electrothermal actuator is that one end of the beam is connected to a fixed end and the other is connected to sliding guide or a central shaft [18]. With this boundary condition, the maximum buckling load can be derived [21] as

$$F_{\text{act}} \leqslant F_{\text{buckling}} = 2n\frac{\pi^2 EI}{L^2}\sin\theta \quad (12)$$

where F_{buckling} is the critical buckling load. From equations (3) and (12), the beam width (*W*) can be given as

$$W \geqslant \sqrt{\frac{12\alpha \Delta T_{\text{ave}}}{n\pi^2}}L. \quad (13)$$

If *L* is assumed to be 1000 μm, from equation (13), *W* should be wider than 9.9 μm to prevent buckling before the actuator generates its maximum force. In addition, *W* should be narrower than *T* to avoid any out-of-plane buckling in operation.

From equations (2), (3), (7) and (10), U_{plat} in equation (1) can be rewritten as

$$U_{\text{plat}} = \left(\frac{L_1}{L_2}\right)\frac{2\alpha n EWT\sin\theta}{3k\rho\left\{2\left(\sin^2\theta + \cos^2\theta\frac{12I}{AL^2}\right)\frac{EA}{L} + \left(\frac{L_1}{L_2}\right)^2\frac{m}{L_1^2 C_z}\right\}}V^2.$$

$$\quad (14)$$

Equation (14) shows a relationship between output displacement of the platform and the driving voltage. Based on equation (14) and the two design considerations on thermal and buckling issues, design parameters of the actuator and the flexure hinge were selected and are listed in table 1. The chip size of the *XY* stage is 7000 μm $\times$ 3500 μm and can generate at least 50 μm in the *X*- and *Y*-axes, respectively. Equation (14) is plotted and compared with the experiment results in figure 7(*a*).

3. Finite element analysis of the *XY* stage

A series of finite element analysis (FEA) simulations are processed in ANSYS[1] 11.0 in order to predict the thermal
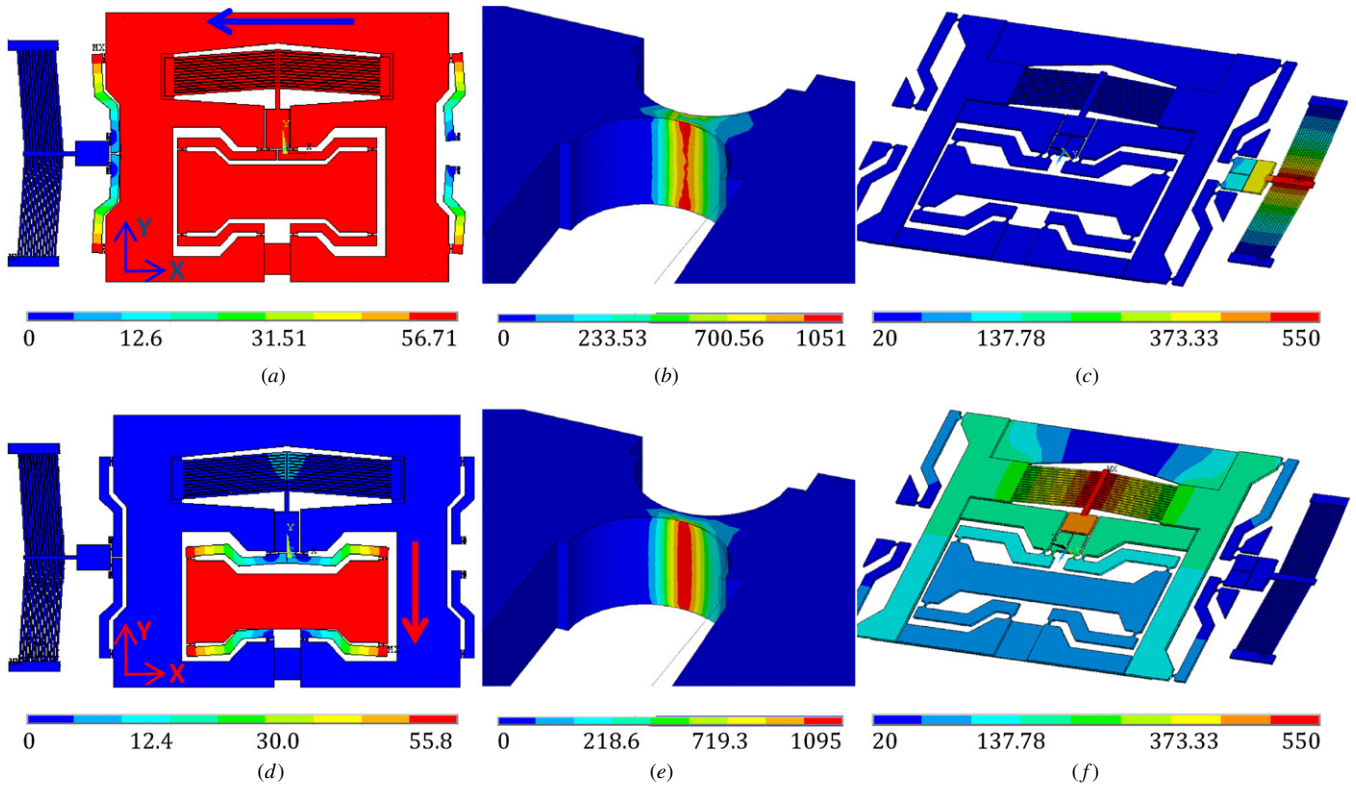
Figure 5. FEA of the proposed *XY* stage: (*a*) displacement in *X*-axis; (*b*) von Mises stress of a flexure hinge; (*c*) temperature distribution when the maximum temperature of the *X* stage is 550 °C; (*d*) displacement in the *Y*-axis; (*e*) first principal stress on a flexure hinge; (*f*) temperature distribution when the maximum temperature of the *Y* stage is 550 °C.

Table 2. Material properties of silicon.

Material properties	Value
Young's modulus	130 GPa
Poisson's ratio	0.28
Resistivity	$-4.72 \times 10^{-7}\,T + 4 \times 10^{-4}\,\Omega$ m
Coefficient of thermal expansion	$3 \times 10^{-9}\,T + 3 \times 10^{-6}\,(°C^{-1})$
Thermal conductivity (T is in °C)	$5 \times 10^{-4}\,T^2 - 0.4706T + 164.15$ W $(m\,°C^{-1})$
Yield strength	7 GPa

and structural behavior of the proposed design. The material properties used in the FEA are described in table 2. For appropriate range of the driving voltage, low resistivity SOI wafers were used for the device fabrication and the resistivity was measured from them.

Boundary conditions and assumptions applied to the FEA on electrical, thermal and mechanical fields are as follows:

(a) Electrical analysis: An electrical potential difference is applied to both ends of an electrothermal actuator. When one is in motion, the other electrothermal actuator is set to be electrically isolated.
(b) Structural analysis: The ends of the outermost four flexures and both ends of the actuator in the *X* stage are assumed to be fixed.
(c) Thermal analysis: The four ends of flexure hinges and both ends of the actuator in the *X* stage are assumed to be at room temperature of 20 °C. For a range of motion

analysis, only heat conduction thermal energy transfer is included in the FEA model. For thermal distribution analysis, both conduction and natural convection heat transfer are included. Radiation heat transfer is ignored.

Figures 5(*a*) and (*d*) show the FEA results of the moving displacements under the temperature which is below 550 °C. Results showed that the *X* stage generates displacement of 51.41 μm at the temperature of 546 °C, and the *Y* stage generates 54 μm under the peak temperature of 478 °C. With the displacements greater than 50 μm, FEA revealed that von Mises stress and the first principal stress on the flexure hinge are less than 1.1 GPa and are shown in figures 5(*b*) and (*e*). These values indicate that no structural failure is expected at the flexure hinges with 50 μm displacement since the known yield strength of silicon is 7 GPa.

The temperature distribution over the stage is also obtained when each actuator is in operation. Figures 5(*c*) and (*f*) depict the temperature distributions of the stage, when either the maximum temperature of the actuator in the *X* stage or the *Y* stage is at 550 °C. The two temperature distributions demonstrate that the two actuators are thermally isolated from each other. But due to different thermal boundary conditions, the *Y* stage tends to stay at higher temperatures than the *X* stage. In addition, figure 5(*f*) shows that the temperature of the platform in the *Y* stage rises up to 130 °C when the maximum temperature of the actuator in the *Y* stage is at 550 °C. Since this temperature rise at the platform was predicted under the maximum actuation condition, the usual temperature of the platform should be less than 100 °C.
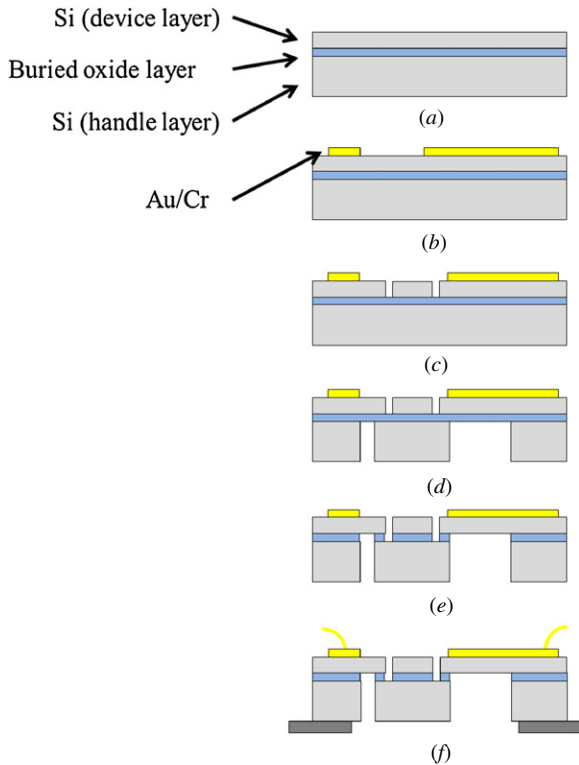
Figure 6. Fabrication sequence of SOI wafer for the *XY* stage: (*a*) a SOI wafer as a starting material; (*b*) metal deposition for electrical connections; (*c*) device layer etching by DRIE; (*d*) handle layer etching with DRIE; (*e*) removal of the buried oxide layer using buffered hydrofluoric acid (BHE); (*f*) installation with bottom spacer and wire bonding.

4. Fabrication of the MEMS *XY* stage

The fabrication process for the proposed MEMS *XY* stage is schematically described in figure 6. A 30 μm thick device layer (upper thin gray area in figure 6(*a*)) is used for the main device structures and a 400 μm thick handle layer (lower thick gray area in figure 6(*a*)) is utilized as a backside supporting structure. A 2 μm thick buried oxide layer (blue thin strip in figure 6(*a*)) is placed between the two silicon layers. The whole process follows silicon-on-insulator multi-user multi-processes (SOIMUMPs) [17]. For reliable electrical connection, a layer of 10 nm of chrome and 700 nm of gold are deposited. The fabrication process consists of four steps—metal layer deposition, DRIE of the device layer, DRIE of the handle layer and removal of the buried oxide layer. The two DRIE processes are carried out up to the buried oxide layer from both sides of SOI wafers. Using buffered hydrofluoric acid (B.H.F.), movable structures are released.

5. Experimental characterization of the MEMS *XY* stage

5.1. The range of motion of the MEMS XY stage and its coupled motion error

The range of motion of the MEMS *XY* stage and its coupled motion error were measured with fabricated *X–Y* stages. In this

Table 3. A coupled motion between the *X* and the *Y* stages.

The target stage	Intended motion (μm)	Coupled motion (μm)
The *X* stage	–	0.1006 (0.569%)
The *Y* stage	17.67	–
The *X* stage	20.48	–
The *Y* stage	–	0.0902 (0.44%)

experiment, four metal pads are electrically connected to two DC power supply units (Model 3322A from Agilent[5]). The corresponding *X* and *Y* positions are measured by an optical profiler (VEECO (see footnote 5) NT1100 [22]). It is evident from figure 7(*a*) that both *X* and *Y* stage displacements are greater than 50 μm within the voltage range of 4.75–5.0 V. Repeated tests for displacement to greater than 50 μm length resulted in no permanent damage to the system. From the FEA it is noted that the *Y* stage reached a higher temperature than the *X* stage, which results in longer displacement for the same driving voltage.

The experimental results, FEA and the analytical solutions (from equation (14)) are compared in figure 7(*a*). The FEA result predicts well the *X* stage motion, because the thermal boundary condition applied to FEA is similar with the *X* stage. The analytical result with constant resistivity shows a lower slope curve than the experimental result. The constant resistivity is an average of the resistivity from room temperature to 550 °C, which is not sufficiently accurate to predict the whole range of motion. But, the analytical result with linearly varying resistivity showed a similar trend with the *Y* stage displacement. This similarity can be explained as follows: equation (14) takes into account only conduction heat transfer which provides a higher slope than the *X* stage motion and the *Y* stage is connected to heat sink via the *X* stage.

The coupled motions between the *X* and the *Y* stages were measured with our intensity-based laser reflectometer. The intensity of the reflected light from the moving edge of the platform was measured. To get the relationship between the reflected intensity and the actual displacement, a calibration test is performed by measuring similar displacements with a commercially available nano-positioning stage equipped with embedded *X–Y* displacement sensors (P-733.3 XYZ Piezo-Nanopositioning Stage [23]). With the calibration completed, the coupled motions by the *X* and the *Y* stages were measured and plotted in figures 7(*b*) and (*c*). From figure 7(*b*) it is evident that for a 20.48 μm motion of the *X* stage (a blue curve), very negligible coupled motion which is less than 0.5% was measured and is depicted in the red line in figure 7(*b*). The measured coupled motion for the *Y* stage movement of 17.67 μm was less than 0.6% of the original *Y* motion. All these results are summarized in table 3 and the coupled motion of the proposed MEMS *XY* stage is well below 0.6%.
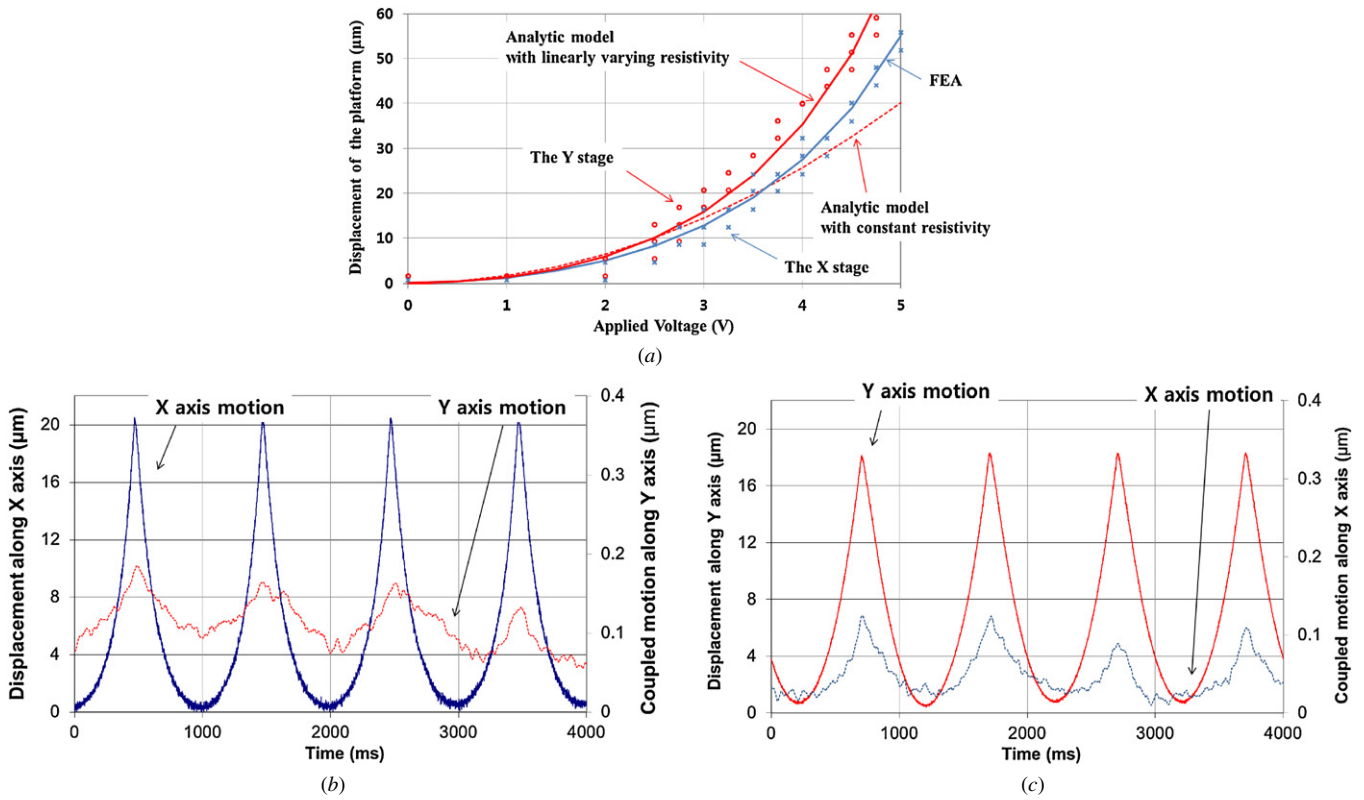
Figure 7. Experiments with fabricated *XY* stages: (*a*) range of motion as a function of driving voltage; (*b*) displacement along the *X*-axis and coupled motion as a function of the elapsed time; (*c*) displacement along the *Y*-axis and coupled motion as a function of the elapsed time (the displacement along the *X*-axis is in blue and along the *Y*-axis is in red).
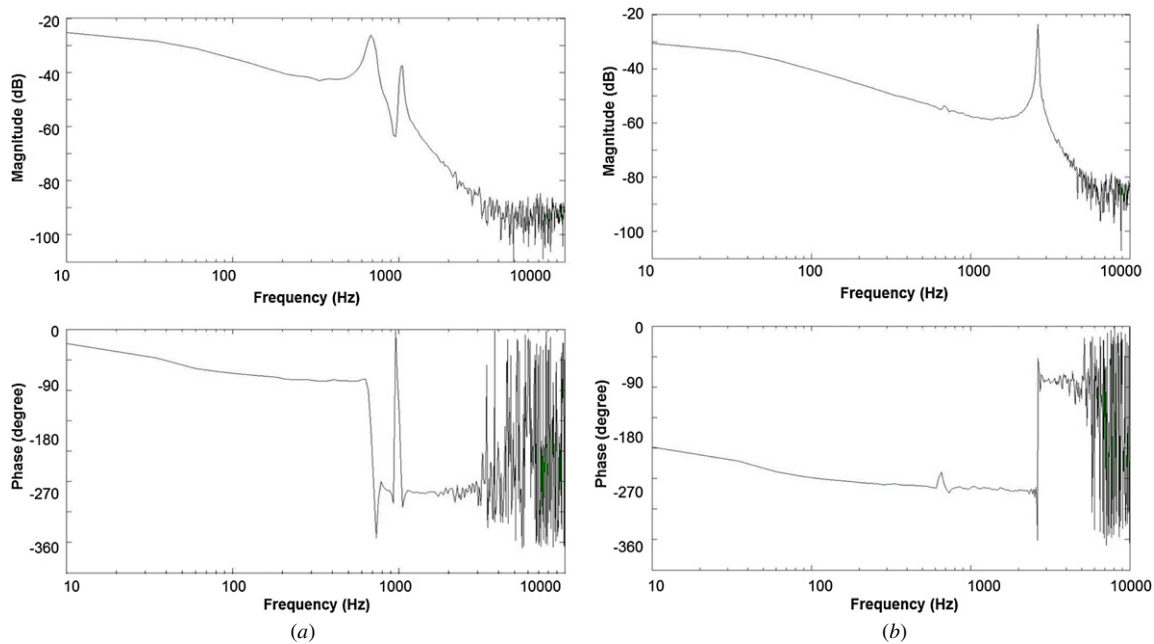

Figure 8. Frequency response bode diagram: (*a*) the *X* stage; (*b*) the *Y* stage.

5.2. The frequency response of the proposed XY stage

The frequency response of the proposed *XY* stage was also measured experimentally along the *X*- and *Y*-axes. The frequency responses were recorded by an Agilent (see footnote 5) Fast-Fourier-Transform (FFT) analyzer when each stage was in operation. More details on frequency response measurements are given elsewhere [24]. The first resonance frequency of the *X* stage occurred at 0.71 kHz and of the *Y* stage at 2.63 kHz as shown in figure 8. The frequency difference between the two stages can be explained by the platform size difference and the mass of the backside supporting frame
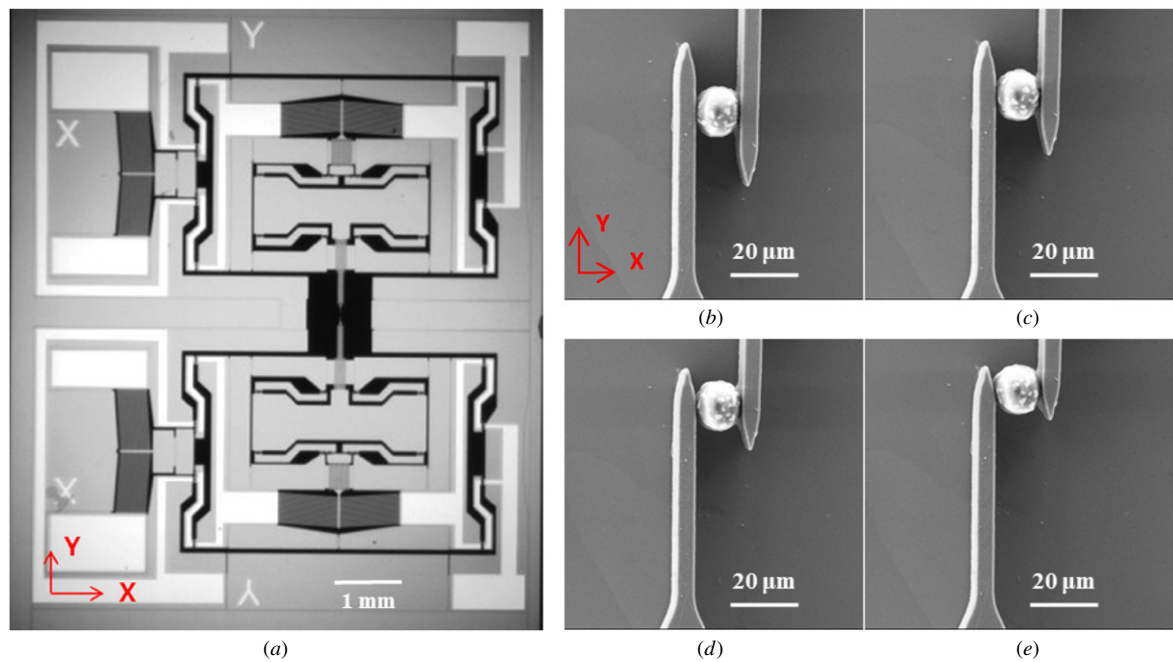
Figure 9. A multifinger manipulation system: (*a*) 2 × 1 layout with two stages; (*b*) gripping a 14.8 μm sized micro particle; (*c*)–(*e*) rotating and moving the particle by controlling the motion of the two fingers.

beneath the *X* stage. Due to these reasons, the first resonance frequency of the *X* stage is relatively lower than that of the *Y* stage. At low frequency, less than 100 Hz, the frequency response shows a slow decrement, which is expected for an electrothermal actuator.

6. The multiprobe finger manipulation system

To verify the usability of the proposed system a multiprobe finger manipulation was investigated. The manipulation system is composed of two *XY* stages and is shown in figure 9(*a*). A finger probe is extended from the platform in each stage to the workspace. The probe ends are facing each other and located to have a 50 μm by 50 μm workspace. From this layout, the two probes can approach to each other along the *Y*-axis and move together along the *X*-axis. Two fingers meet each other at any position inside the workspace and operate together for the manipulation operation. With this layout, it was possible to pick up a micro-scale object, rotate it along the *z*-axis and position it within the workspace. The manipulation of a micro-sized particle was successfully demonstrated and several of the live images were captured inside a scanning electron microscope (SEM). Figure 9(*b*) shows a SEM picture of the two fingers gripping a 15 μm sized polypropylene particle. After the gripping, this object was rotated and translated by moving two fingers along the *Y*-axis, as shown in figures 9(*c*)–(*e*). In addition, the gripped objects can be moved along the *X*- and *Y*-axes by moving the two fingers in a coordinated fashion.

7. Conclusions

The design, fabrication and testing of a MEMS-based *XY* stage for large stroke and negligible coupled motion

for applications such as micro/nano dynamic metrology, coordinate measurement machine metrology machining, manipulation and assembly were successfully accomplished. For the MEMS *XY* stage, the following features were adopted: (1) modification of the single DOF stage to have more than 50 μm in motion displacement, (2) adopting the nested structure to combine two single DOF stages to build an in-plane two-DOF stage with negligible coupled motion, (3) the electric isolation between two stages to avoid any electrical leakage and (4) embedded electrical connection for the *Y* stage. With these features, the fabricated *XY* stage generated at least 50 μm in displacement in the *Y*-direction. The FEA and the analytic solutions showed that when applying less than 5 V, the status of the electrothermal actuator is below its thermal or buckling limits. With a nested structure, its coupled motion was successfully reduced to 0.6% of the other axis motions. The first resonance frequencies of the *X* stage and the *Y* stage are at 705 Hz and 2.63 kHz, respectively. A successful demonstration on the micro-sized particle with the two fingers actuated by the two neighboring *XY* stages was also presented.

This system can be extended for further applications by embedding or stacking different devices into it. Instead of the *Y* stage, two *X* stages can be employed for extending the motions greater than 100 μm. Additionally one more stage can be embedded into the *Y* stage for three DOF motions or rotational motions. Instead of a *Z* stage, a gripper or embedded sensor can be placed in the platform of the *Y* stage for manipulation.

Acknowledgments

References

[1] Yao Q, Dong J and Ferreira P M 2007 Design, analysis, fabrication and testing of a parallel-kinematic micropositioning *XY* stage *Int. J. Mach. Tools Manuf.* **47** 946–61

[2] Sahu B, Taylor C R and Leang K K 2010 Emerging challenges of microactuators for nanoscale positioning, assembly, and manipulation *J. Manuf. Sci. Eng.* **132** 030917

[3] Kim C H and Kim Y K 1999 Integration of a micro lens on a micro *XY*-stage *Proc. SPIE* **3892** 109–17

[4] Laszczyka K, Bargiela S, Goreckia C, Krężelb J, Dziubana P, Kujawińskab M, Calletc D and Frankd S 2010 A two directional electrostatic comb-drive *X–Y* micro-stage for MOEMS applications *Sensors Actuators* A **163** 255–65

[5] Indermuhle P F, Jaecklin V P, Brugger J, Linder C, de Rooij N F and Binggeli M 1995 AFM imaging with an *xy*-micropositioner with integrated tip *Sensors Actuators* A **47** 562–5

[6] Sun L, Wang J, Rong W, Li X and Bao H 2008 A silicon integrated micro nano-positioning *XY*-stage for nano-manipulation *J. Micromech. Microeng.* **18** 125004

[7] Gorman J J, Kim Y S, Vladar A E and Dagalakis N G 2007 Design of an on-chip microscale nanoassembly system *Int. J. Nanomanuf.* **1** 710–21

[8] Duc T C, Lau G K and Sarro P M 2008 Polymeric thermal microactuator with embedded silicon skeleton: part II-fabrication, characterization, and application *J. MEMS* **17** 823–31

[9] Mukhopadhyay D, Dong J, Pengwang E and Ferreira P 2008 A SOI-MEMS-based 3-DOF planar parallel-kinematics nanopositioning stage *Sensors Actuators* A **147** 340–51

[10] Dong J and Ferreira P M 2009 Electrostatically actuated cantilever with SOI-MEMS parallel kinematic *XY* stage *J. MEMS* **18** 641–51

[11] Gao P, Swei S-M and Yuan Z 1999 A new peizo-driven precision micropositioning stage utilizing flexure hinges *Nanotechnology* **10** 394–8

[12] Wright J A, Tai Y C and Chang S C 1997 A large-force, fully-integrated MEMS magnetic actuator *Solid State Sensors and Actuators Int. Conf. 16–19* vol 2 pp 793–6

[13] Bergna S, Gorman J J and Dagalakis N G 2005 Design and modeling of thermally actuated MEMS nanopositioner *IMECE'2005: Proc. ASME Int. Mechanical Engineering Congress and Exposition (Orlando, FL, USA)*

[14] Paros J M and Weisbord L 1965 How to design flexure hinges *Mach. Des.* **37** 151–6

[15] Yang S H, Kim Y S, Purushotham K P, Yoo J M, Choi Y M and Dagalakis N G 2010 AFM characterization of nanopositioner in-plane stiffnesses *Sensors Actuators* A **163** 383–7

[16] Howatson A M, Lund P G and Todd J D 1991 *Engineering Tables and Data* 2nd edn p 41

[17] Miller K, Cowen A, Hames G and Hardy B *SOIMUMPs Design Handbook revision 4.0* http://www.memscap.com/ mumps/documents/SOIMUMPs.dr.v4.pdf

[18] Zhu Y, Corigliano A and Espinosa H D 2006 A thermal actuator for nanoscale *in situ* microscopy testing: design and characterization *J. Micromech. Microeng.* **16** 242–53

[19] Baker M S, Plass R A, Headley T J and Walraven J A 2004 Final report: compliant thermomechancial MEMS actuators LDRD www.mems.sandia.gov/tech-info/doc/ thermal_actuator_SAND.pdf

[20] Luo J L, Flewitt A J, Spearing S M, Fleck N A and Milne W L 2005 Three types of planar structure microspring electro-thermal actuators with insulating beam constraints *J. Micromech. Microeng.* **15** 1527–35

[21] Jones R M 2008 *Buckling of Bars, Plates, and Shells* pp 73–5

[22] DMEMS Dynamic MEMS Measurement Option for Wyko NT1100 Optical Profilers http://www2.veeco.com/ pdfs.php/396

[23] PI Piezo Nano Positioning 2009 2-62-2-63 www.physikinstrumente.com/en/products/prdetail. php?sortnr=201250

[24] Gorman J J, Kim Y S and Dagalakis N G 2006 Control of MEMS nanopositioners with nano-scale resolution ASME *Proc. of the ASME Int. Mechanical Engineering Conf. and Exhibition (Chicago, USA)*